



저작자표시-비영리-동일조건변경허락 2.0 대한민국

이용자는 아래의 조건을 따르는 경우에 한하여 자유롭게

- 이 저작물을 복제, 배포, 전송, 전시, 공연 및 방송할 수 있습니다.
- 이차적 저작물을 작성할 수 있습니다.

다음과 같은 조건을 따라야 합니다:



저작자표시. 귀하는 원저작자를 표시하여야 합니다.



비영리. 귀하는 이 저작물을 영리 목적으로 이용할 수 없습니다.



동일조건변경허락. 귀하가 이 저작물을 개작, 변형 또는 가공했을 경우에는, 이 저작물과 동일한 이용허락조건하에서만 배포할 수 있습니다.

- 귀하는, 이 저작물의 재이용이나 배포의 경우, 이 저작물에 적용된 이용허락조건을 명확하게 나타내어야 합니다.
- 저작권자로부터 별도의 허가를 받으면 이러한 조건들은 적용되지 않습니다.

저작권법에 따른 이용자의 권리는 위의 내용에 의하여 영향을 받지 않습니다.

이것은 [이용허락규약\(Legal Code\)](#)을 이해하기 쉽게 요약한 것입니다.

[Disclaimer](#)

공학석사 학위논문

**Understanding the degradation
mechanisms of layered lithium nickel-
cobalt-manganese oxides as a cathode
material for lithium ion batteries**

리튬 이온 전지용 양극재 리튬 니켈 코발트 망간
산화물에 대한 열화 메커니즘 분석 연구

2014 년 2 월

서울대학교 대학원

재료공학부

정 성 균

Understanding the degradation mechanisms of layered lithium nickel- cobalt-manganese oxides as a cathode material for lithium ion batteries

리튬 이온 전지용 양극재 리튬 니켈 코발트 망간
산화물에 대한 열화 메커니즘 분석 연구

지도 교수 강 기 석

이 논문을 공학석사 학위논문으로 제출함

2013 년 12월

서울대학교 대학원

재료공학부

정 성 균

정 성 균의 석사 학위论문을 인준함

2013 년 12 월

위 원 장 _____ 류 한 일 (인)

부위원장 _____ 강 기 석 (인)

위 원 _____ 박 병 우 (인)

Abstract

Understanding the degradation mechanisms of layered lithium nickel-cobalt-manganese oxides as a cathode material for lithium ion batteries

Jung, Sung-Kyun

Department of Material Science and Engineering

College of Engineering

The Graduate School

Seoul National University

$\text{LiNi}_x\text{Co}_y\text{Mn}_z\text{O}_2$ (NCM, $0 < x, y, z < 1$, $x+y+z=1$) has become one of the promising cathode materials for next generation lithium ion batteries due to its high capacity and the cost effectiveness compared to LiCoO_2 . However, the high voltage operation of NCM (> 4.3 V) that is required for a higher capacity inevitably accompanies more rapid capacity fading over cycles. Here, the degradation mechanisms of $\text{LiNi}_{0.5}\text{Co}_{0.2}\text{Mn}_{0.3}\text{O}_2$ are investigated during

cycling at various charge cut-off voltage conditions. The surface crystal structure of the $\text{LiNi}_{0.5}\text{Co}_{0.2}\text{Mn}_{0.3}\text{O}_2$ suffers from an irreversible transformation, and the type of a surface structure varies depending on the cut-off voltage condition. The surface of the pristine rhombohedral phase transforms into a mixture of spinel and rock salt phases which contributes to a gradual increase in charge transfer resistance. Furthermore, the formation of the rock salt phase is more dominant with a higher voltage operation (~ 4.8 V), which is due to the highly oxidative environment that triggers the oxygen loss from the surface of the material. The presence of the ionic insulating rock salt phase may cause a sluggish kinetics, thus, deteriorate the capacity retention. It implies that the prevention of the surface structural degradation can provide a way to the high capacity and stable cycle life of $\text{LiNi}_{0.5}\text{Co}_{0.2}\text{Mn}_{0.3}\text{O}_2$ for high voltage operation.

Keywords: degradation mechanism; layered structure; lithium ion battery; NCM; $\text{LiNi}_{0.5}\text{Co}_{0.2}\text{Mn}_{0.3}\text{O}_2$

Student Number: 2012-20633

Contents

Abstract	i
Contents	iii
List of Tables	v
List of Figures	vi
Chapter 1 Introduction	1
1.1 Motivation and outline.....	1
Chapter 2 Reaserch backgrounds	4
2.1. Introduction to lithium rechargeable batteries.....	4
2.2. Layered structure lithium transition metal oxide.....	8
Chapter 3 Experimental	14
3.1. Characterization of $\text{LiNi}_{0.5}\text{Co}_{0.2}\text{Mn}_{0.3}\text{O}_2$	14
3.2. Electrochemical analysis	14
3.3. Ex-situ structural analysis	15
3.3.1. X-ray diffraction	15
3.3.2. Transmission electron microscope	16

Chapter 4 Results and discussion	17
4.1. Characterization of as-prepared $\text{LiNi}_{0.5}\text{Co}_{0.2}\text{Mn}_{0.3}\text{O}_2$	17
4.2. Electrochemical degradation of $\text{LiNi}_{0.5}\text{Co}_{0.2}\text{Mn}_{0.3}\text{O}_2$	19
4.3. Structural analysis	26
4.4. Effect of current rate on structural changes	41
4.5. Degradation mechanisms of $\text{LiNi}_{0.5}\text{Co}_{0.2}\text{Mn}_{0.3}\text{O}_2$	44
 Chapter 5 Conclusion	 49
 Reference	

List of Tables

Table 1. Concentration of Ni, Co and Mn ions in electrolyte after 50 cycles at different cutoff voltages.

Table 2. Resistance values of as-prepared and cycled samples obtained from equivalent circuit in Figure 7b.

Table 3. Lattice parameters of as-prepared and cycled samples of Figure 11.

List of Figures

Figure 1. Schematic figure of a lithium-ion battery composed by the graphite and LiCoO_2 as electrode materials.

Figure 2. Oxygen stacking sequences of O3 and O1 type of materials. (H1-3; hybridization of O3 and O1 structure)

Figure 3. Charge and discharge curves of a $\text{Li/LiNi}_{1/3}\text{Co}_{1/3}\text{Mn}_{1/3}\text{O}_2$ cell operated at a rate of 0.17 mA cm^{-2} in voltages between 2.5 and 5.0 V at 30°C

Figure 4. Charge and discharge curves of a $\text{Li/LiNi}_{0.5}\text{Co}_{0.2}\text{Mn}_{0.3}\text{O}_2$ cell operate at a 0.1C rate in voltages between 2.5 and 4.3 V at 25°C

Figure 5. X-ray diffraction (XRD) pattern of $\text{LiNi}_{0.5}\text{Co}_{0.2}\text{Mn}_{0.3}\text{O}_2$ indexed based on the $\text{R}\bar{3}\text{m}$. The R factors are $R_p = 1.39\%$, $R_t = 1.69\%$, and $R_F = 2.69\%$. The figure inset shows transmission electron microscopy (TEM) images and the diffraction pattern of the single particles.

Figure 6. (a) Cycle performance and (b) discharge capacity retention at various cutoff voltages during 50 cycles.

Figure 7. (a) Electrochemical impedance spectroscopy (EIS) profiles of electrodes in coin cells of the as prepared sample and samples after 50 cycles. (b) Equivalent circuit for electrodes. R_s : solution resistance; R_f : surface film resistance; R_{ct} : charge transfer resistance.

Figure 8. Recovered capacity retention after 50 cycles at a slower current rate (10 mA g^{-1}).

Figure 9. X-ray diffraction (XRD) patterns of the as-prepared electrode

before and after 50 cycles.

Figure 10. Magnified x-ray diffraction (XRD) patterns of Figure 9 around $2\theta = 18 \sim 19^\circ$

Figure 11. Lattice parameter changes of the electrodes as-prepared and after 50 cycles.

Figure 12. Diffraction patterns at the zone axis $[-1-21]_R$ after 50 cycles under 3.0–4.8 V conditions for the (a) bulk and (b) surface regions. The figure insets show bright intensity maps of the spots along yellow and blue lines. R represents a peak from the layered phase; S represents peaks from the spinel phase.

Figure 13. High-resolution transmission electron microscopy (HR-TEM) images and fast Fourier transforms (FFT) after 50 cycles under 3.0–4.8 V conditions. (a) Lattice image of the surface region where (b)–(e) correspond to the FFTs of Regions 1–4, respectively. (11-1)c is the diffraction spot of the rock salt phase of the metal monoxide

Figure 14. Electron energy loss spectroscopy (EELS) at the O–K edge of the as-prepared sample, the 4.5-V cutoff sample, and the 4.8-V cutoff sample. The spectra were measured within a few nanometers of the surface.

Figure 15. HR-TEM images and FFTs after 50 cycles under 3.0–4.5 V conditions. (a) Lattice image of the surface region where (b)–(e) correspond to the FFTs of Regions 1–4, respectively.

Figure 16. Diffraction patterns at zone axis $[-1-21]_R$ after 50 cycles for the voltage range of 3.0–4.3 V for the (a) bulk and (b) surface regions.

Figure 17. (a) High-resolution transmission electron microscopy (HR-TEM) images and fast Fourier transforms (FFT) after 50 cycles in the 3.0–4.3 V range. (b) and (c) FFTs of Regions 1 and 2, respectively

Figure 18. (a) Cycle performance and (b) discharge capacity retention at 1000 mA g⁻¹ in 3.0–4.5 V voltages during 50 cycles.

Figure 19. (a) HR-TEM image at the zone axis [010]_R after 50 cycles at 1000 mA g⁻¹ in the 3.0–4.5 V range and (b), (c) FFT of the region 1, 2.

Figure 20. (a) Diffraction patterns of the zone axis [010]_R after 50 cycles in the 3.0–4.8 V range. (b) HR-TEM image and (c) FFT of the (b) region. The yellow circle shows the position of the O1 phase (-202) in which no spot was shown. The red circle corresponds to the position of the spinel structure.

Figure 21. Degradation mechanisms of LiNi_{0.5}Co_{0.2}Mn_{0.3}O₂ and phase transformation after cycle tests under high-voltage conditions.

Chapter 1. Introduction

1.1 Motivation and outline

Demands for Li-ion batteries are currently extending from portable electronics to large scale applications such as energy storage systems (ESS) and electric vehicles (EVs).^[1, 2] Higher energy density combined with longer cycle life is one of the key requirements that need to be addressed in these new applications.^[3, 4] Layered lithium transition metal oxides have served as the most important cathode materials for high energy batteries due to the large theoretical capacity (~ 280 mAh/g) compared with those of olivine (~ 170 mAh/g) or spinel (~ 150 mAh/g) materials.^[5-7] LiCoO_2 which delivers high working voltage (~ 3.9 V) with excellent rate capability has been the most widely used in commercial batteries. However, the limitations of LiCoO_2 such as a small practical capacity (~ 150 mAh/g), unreliable safety and high cost of cobalt have led researchers to focus on other layered materials with less cobalt. While the single component systems, including LiMnO_2 and LiNiO_2 also suffer from intrinsic problems such as poor cyclability and rate capability as well as the complexity in preparation, three component layered $\text{LiNi}_x\text{Co}_y\text{Mn}_z\text{O}_2$ (NCM, $0 < x, y, z < 1$) could exhibit promising

electrochemical properties depending on the composition of Ni, Co and Mn in the structure.^[7-12] Generally, high Ni contents in the NCM contribute to higher capacity at the expense of safety and complexity in preparation; high Mn contents enhance the structural stability at the expense of capacity; and high Co contents improve the rate performance and processability at the expense of cost.

Two representative NCM layered materials have so far been successfully adopted in commercial lithium ion batteries; $\text{LiNi}_{1/3}\text{Co}_{1/3}\text{Mn}_{1/3}\text{O}_2$ (NCM111) and $\text{LiNi}_{0.5}\text{Co}_{0.2}\text{Mn}_{0.3}\text{O}_2$ (NCM523). Less use of Co in these materials compared to LiCoO_2 has contributed to reduce the cost and improve the safety in the new battery system. Nevertheless, the enhancement of energy density has not been sufficiently achieved even though NCM layered materials are capable of delivering higher capacity due to larger range of reversible Li insertion and extraction. To acquire high capacity from NCM layered material, operation at high voltage ranges (~ 4.5 V) is required, which inevitably accompanies more rapid capacity fading over cycles. While recent efforts such as various surface coatings of NCM materials have improved the high-voltage cycling stability^[13-20], it is still lack of understanding on the origin of the accelerated degradation of cycle performance during high-voltage operation.

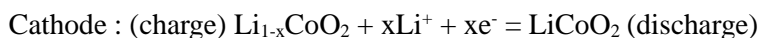
In this study, we investigate the degradation mechanisms of a $\text{LiNi}_{0.5}\text{Co}_{0.2}\text{Mn}_{0.3}\text{O}_2$ (NCM523) cathode, one of the most important commercialized NCM materials, as a function of charge cut-off voltages with detailed structural analyses in both respects of bulk and surface. It is shown that the aspect of surface structural degradation is critically affected by the cut-off voltage, which results in the formation of ionic insulating layer on the surface of NCM, thus, reduce the capacity retention.

Chapter 2. Research backgrounds

2.1. Introduction to lithium rechargeable batteries

After the discovery of voltaic cell in 1800, there are two innovative progresses in battery technology. One is development from primary to secondary battery which is able to be charged and discharged. The other is the increase of operation voltage to 3 V and 4 V. Lithium rechargeable battery works at operation voltage of around 3.7 V and shows energy density about 150 Wh kg⁻¹, much higher than those of other batteries.

Lithium rechargeable batteries consist of several components which are cathode, anode, electrolyte and separator. Lithium ion is used as charge carrier in electrolyte during charge and discharge, thus, cathode and anode are composed of materials which can accept the lithium ion in their crystal structure. In conventional Li rechargeable battery, LiCoO₂ is used as a cathode due to the good cyclability and electrical conductivity, and graphite is used as an anode due to its safety and good cyclability. The electrochemical reaction taking place between the two electrodes are described below:



Anode : (discharge) $\text{Li}_x\text{C}_6 = x\text{Li}^+ + xe^- + \text{C}_6$ (discharge)

Equation 1, 2 and figure 1 explains the operation principles of lithium rechargeable battery. During charge, Li ions are extracted out of the cathode(LiCoO_2), diffuse through the electrolyte, and are inserted into the anode(graphite). At the same time, the electrons flow from cathode to anode through the external circuit which connect between the two electrodes. During discharge, the overall reaction turn to opposite direction, Li ions and electron diffuse from anode to cathode through the electrolyte and circuit.

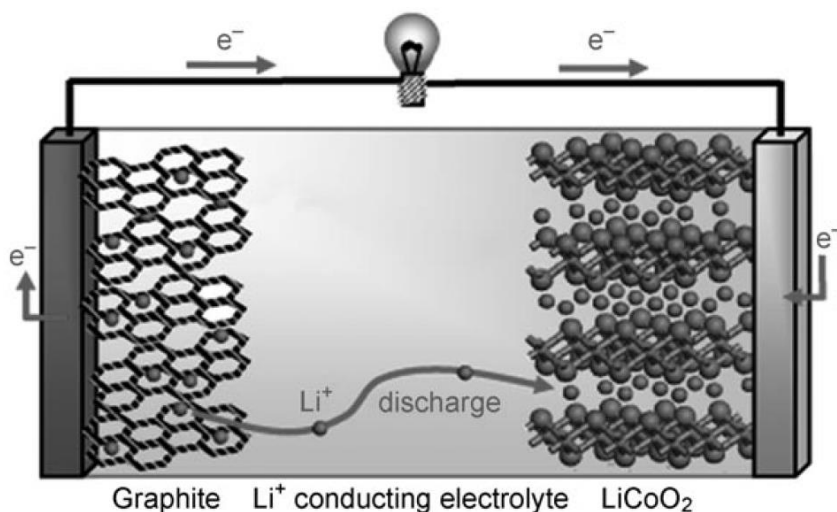


Figure 1. Schematic figure of a lithium-ion battery composed by the graphite and LiCoO_2 as electrode materials.^[21]

During the charge and discharge, the energy can be stored in the battery is determined by the capacity and operation voltage. The capacity is proportional to the amount of lithium can be extracted and inserted into the structure of cathode and anode materials. The operation voltage of lithium rechargeable batteries is established by the difference in the chemical potential of lithium between the cathode and anode. Thus, the cathode materials which have low chemical potential of lithium and the anode materials which have high chemical potential of lithium have to be selected to design the large energy storage battery system.

The choice of electrode materials is very important for better performance of lithium rechargeable battery because the electrochemical reaction in a battery is dependent on the electrode materials. The key parameters for electrode materials are energy density, power density, cycle life, cost and safety.

Energy density is classified as gravimetric and volumetric density. The gravimetric density is defined as the available energy per unit weight and the other is volumetric density is defined as the energy per unit volume. The gravimetric or volumetric energy density is product of voltage and specific capacity. The specific capacity of the electrode material is calculated by the equation 3.

$$\text{Specific capacity} = \frac{\Delta x \cdot F}{M} \times \frac{1000}{3600} \quad [\text{mAh/g}] \quad \dots\dots\dots \text{equation 3}$$

The specific capacity is proportional to the amount of lithium (Δx) which participates in the electrochemical reaction reversibly. M is the molar mass of the electrode material.

The power density is also called as rate capability which is defined as the available power per unit weight. The value of power density can be calculated by the product of current and voltage of the battery cell and it can be simply thought as the energy density divided by the discharging time. The power density is dependent on the impedance of the battery aroused by numerous factors such as Li diffusion in crystal structure, electronic/ionic conductivity, cell geometry and so on.

The cycle life means the number of charge and discharge cycles that the specific capacity decrease below a certain value. The cycle life is affected by the structural stability of electrode materials as function of Li contents in the structure and the volume change during charge and discharge also affects to the cycle life of the battery cell.

2.2 Layered structure lithium transition metal oxide

In Li rechargeable batteries, the materials which have high voltage and high energy density are required as cathode materials. To satisfy the requirements, the materials which are light, and also can accommodate large amounts of Li in their closed packed structure are recommended. The representative materials have the conditions are the materials group which have LiMX_2 chemical composition (M: transition metal, X: chalcogenide such as O and S). LiMX_2 materials are simply composed of one transition metal cation and two chalcogenide anions. The 3d transition metal ion is usually used as cation in cathode materials because of the relatively higher voltage compared to the 4d or 5d transition metal ions. Among the anions in LiMX_2 , oxygen is better than other chalcogenides or halogen for contribution to the structural stability during the oxidation and reduction reaction as building block of the materials.

Among the various LiMX_2 type of materials, transition metal oxides (LiMO_2) with a layered structure (O3 type) materials are widely researched and used as cathode. The layered lithium transition metal oxide consists of closed-packed oxygen plane frameworks. The oxygen planes are stacked in a sequential way of ABCABC... (Figure 2). Between the oxygen planes, the

transition metal ions and lithium ions are located in the octahedral site alternately as layer by layer ($\dots -O_{(A)}-Li-O_{(B)}-TM-O_{(C)}-Li-O_{(A)}-TM-O_{(B)}- \dots$). Therefore the Li ions are located in the structure as a plane and moves in and out of the material through the two dimensional channel.

The representative materials of O3 type layered transition metal oxides are $LiCoO_2$ and $LiNiO_2$. $LiCoO_2$ is the positive electrode material that was used in the one of the first commercially successful rechargeable Li batteries, and has been used mostly widely until now. $LiCoO_2$ has good power capability due to the high ionic/electronic conductivity and long cycle life, however, only half of the Li are available for reversible charge and discharge reaction. When above the half of the Li extracted from the $LiCoO_2$, the structure changes from O3 to O1 type of material which was not available for reversible electrochemical reaction (Figure 2).

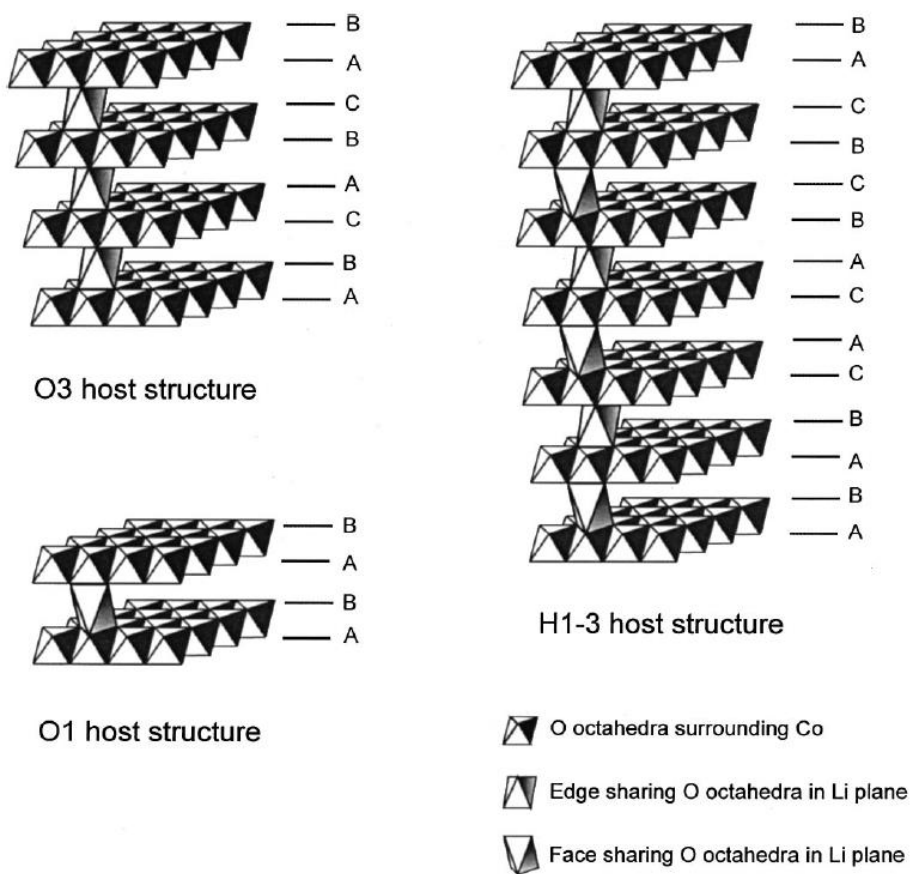


Figure 2. Oxygen stacking sequences of O3 and O1 type of materials. (H1-3; hybridization of O3 and O1 structure)^[22]

LiNiO₂ is another representative material of O3 type layered transition metal oxides with LiCoO₂. LiNiO₂ has possibility of more than half of the Li are available for charge and discharge reaction. However, stoichiometric LiNiO₂ is extremely hard to synthesize and the Li_{1-x}Ni_{1+x}O₂ is produced during the synthesize process due to the similar ionic size of Li⁺ (0.76 Å) and Ni²⁺ (0.69 Å) ions. Additional Ni ions in Li_{1-x}Ni_{1+x}O₂ easily occupy the Li site and the Ni in Li site affects to the power capability and cycle life of LiNiO₂ positive electrode material. The electrochemical properties of LiNiO₂ dramatically degrade through the repetitive cycles due to the excess of Ni ions.^[7]

To complement the low capacity of LiCoO₂ and poor power capability and cycle life of LiNiO₂, multi-transition-metal layered oxides such as Li[Ni_{1-x}Co_x]O₂, Li[Ni_{1-x-y}Co_xMn_y]O₂ materials have been investigated.^[23-25] The synergetic effects of each transition metal are effective in terms of specific capacity, rate capability and cycle life. Among the materials which have various compositions, LiNi_{1/3}Co_{1/3}Mn_{1/3}O₂ (NCM111) and LiNi_{0.5}Co_{0.2}Mn_{0.3}O₂ (NCM523) are widely researched. Each transition metal participates on the electrochemical properties of materials. Generally, Ni contents in NCM contribute to higher capacity at the expense of safety and

complexity in preparation; Co contents improve the rate performance and processability at the expense of cost; and Mn contents enhance the structural stability at the expense of capacity.

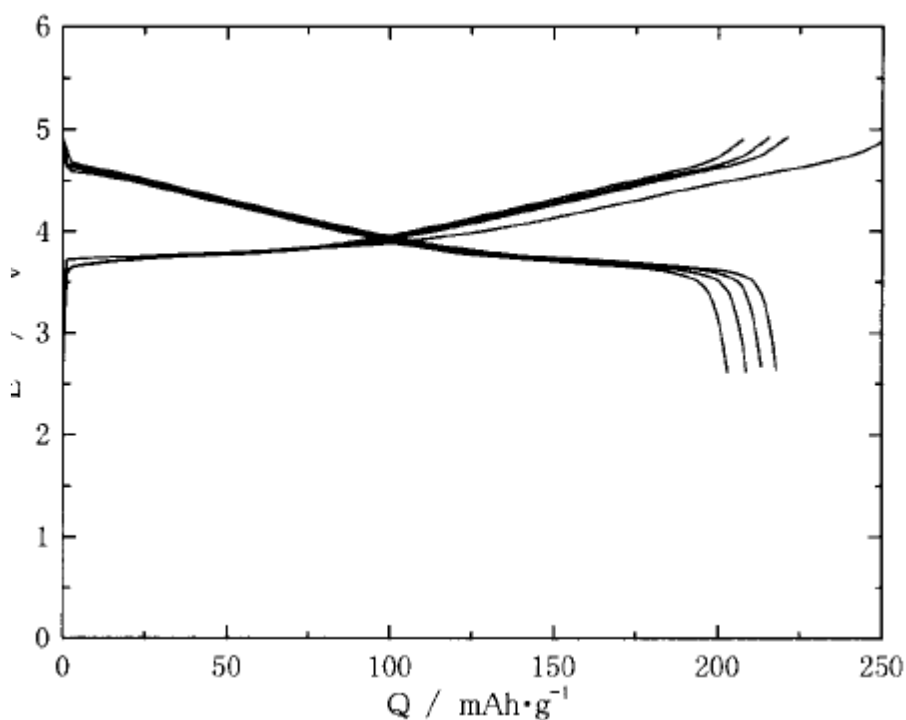


Figure 3. Charge and discharge curves of a $\text{Li/LiNi}_{1/3}\text{Co}_{1/3}\text{Mn}_{1/3}\text{O}_2$ cell operated at a rate of 0.17 mA cm^{-2} in voltages between 2.5 and 5.0 V at 30°C

[10]

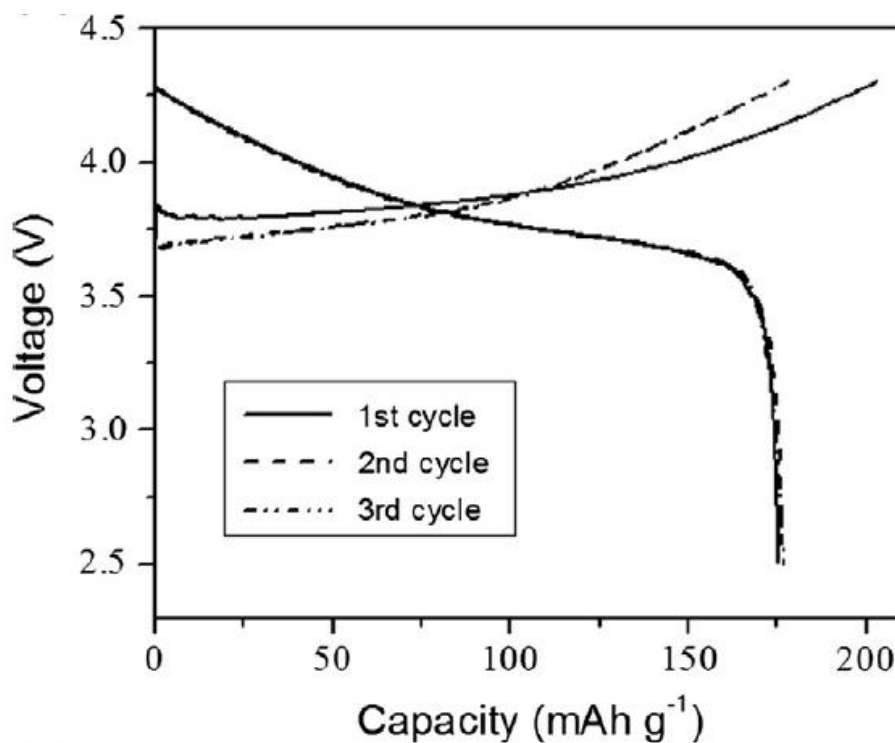


Figure 4. Charge and discharge curves of a Li/LiNi_{0.5}Co_{0.2}Mn_{0.3}O₂ cell operate at a 0.1C rate in voltages between 2.5 and 4.3 V at 25 °C [26]

Chapter 3. Experimental

3.1. Characterization of $\text{LiNi}_{0.5}\text{Co}_{0.2}\text{Mn}_{0.3}\text{O}_2$

The $\text{LiNi}_{0.5}\text{Co}_{0.2}\text{Mn}_{0.3}\text{O}_2$ sample was supplied by Samsung Fine Chemicals (Daejeon, Korea). The powder sample was characterized using a D2 PHASER (Bruker, Bremen, Germany) equipped with Cu-K α radiation ($\lambda = 1.54178 \text{ \AA}$) at a scanning speed $0.2^\circ \text{ min}^{-1}$ in the 2θ range of $10\text{--}70^\circ$. The stoichiometry of the compound was confirmed by inductively coupled plasma atomic emission spectroscopy (ICP-AES; Polyscan 60E; Thermo Jarrell Ash, Franklin, MA, USA). The shape and size of the primary particles were examined using a 200 kV field emission transmission electron microscope (FE-TEM; TechaniTM-F20; FEI, Hillsboro, OR, USA).

3.2. Electrochemical analysis

Test electrodes were fabricated by the following sequence. A slurry of 70 wt% $\text{LiNi}_{0.5}\text{Co}_{0.2}\text{Mn}_{0.3}\text{O}_2$, 20 wt% carbon black (Super-P; Timcal, Bodio, Switzerland), and 10 wt% polyvinylidene fluoride (PVDF) binder, dissolved

in N-methyl-1,2-pyrrolidone (NMP, 99.5%; Sigma-Aldrich, St. Louis, MO, USA), was cast onto aluminum foils using a doctor blade method. NMP was evaporated overnight at 70 °C in a vacuum oven. Coin cells (CR2016; Hohsen, Osaka, Japan) were assembled with the $\text{LiNi}_{0.5}\text{Co}_{0.2}\text{Mn}_{0.3}\text{O}_2$ electrode, Li counter electrode, a separator (2400; Celgard, Tokyo, Japan), and a 1 M solution of LiPF_6 in a mixture of ethyl carbonate/dimethyl carbonate (EC/DMC, 1:1 v/v) in an argon-filled glove box. The galvanostatic charge/discharge profile was measured over the voltage ranges of 3.0–4.3, 3.0–4.5, and 3.0–4.8 V by a potentiogalvanostat (WBCS 3000; WonA Tech, Seoul, Korea) under 110 mA g^{-1} (0.4 C) at room temperature for 50 cycles. After the 50 cycles were completed, electrochemical impedance spectroscopy (EIS) measurements were performed on the tested cells using an impedance analyzer (ZIVE SP2; WonA Tech) at room temperature in the frequency range of 1 MHz to 1 mHz.

3.3. Ex-situ structural analysis

3.3.1. X-ray diffraction

After 50 cycles with different cutoff voltage conditions (3.0–4.3, 3.0–4.5, and 3.0–4.8 V), three electrodes were collected for structural analysis. The fully discharged electrodes were disassembled from coin cells, rinsed with DMC several times, and dried at room temperature in a vacuum oven for X-ray diffraction (XRD) measurements. Lattice parameters of electrodes were determined by the Rietveld method using Fullprof software.^[27]

3.3.2. Transmission electron microscope

For high-resolution transmission electron microscopy (HR-TEM) analysis, the active material was raked out and dispersed in ethanol using a sonicator before being transferred onto a lacey carbon-supported Cu grid. HR-TEM images and energy electron loss spectroscopy (EELS) spectra of the samples were recorded using a 200-kV FE-TEM. EELS spectra were acquired from the outermost surface region within a square area of $\sim 3 \times 3$ nm, with an acquisition time of 2 s. The collection angle and convergence angles were 40 mrad and 30 mrad, respectively. The exposure time of the sample to the electron beam was minimized. O–K edge spectra were collected.

Chapter 4. Results and discussion

4.1. Characterization of as-prepared $\text{LiNi}_{0.5}\text{Co}_{0.2}\text{Mn}_{0.3}\text{O}_2$

The phase purity of NCM523 was firstly confirmed by the XRD (Figure 5). XRD data show a typical pattern of $\alpha\text{-NaFeO}_2$ structure of $R\bar{3}m$ space group. No impurity was detected. Clear peak separation of (006)/(012) and (108)/(110) indicates the well crystalline layered structure.^[28] Lattice parameters were obtained by Rietveld refinement as shown in Figure S1, which agree well with previous reports.^[14] Measured composition of transition metals by ICP-AES was Ni:Co:Mn=0.482:0.222:0.296 comparable to the target composition of NCM523. The primary particle was about 500 nm and composed of single crystal phase as observed by the TEM diffraction pattern (DP). (Inset figure of Figure 5)

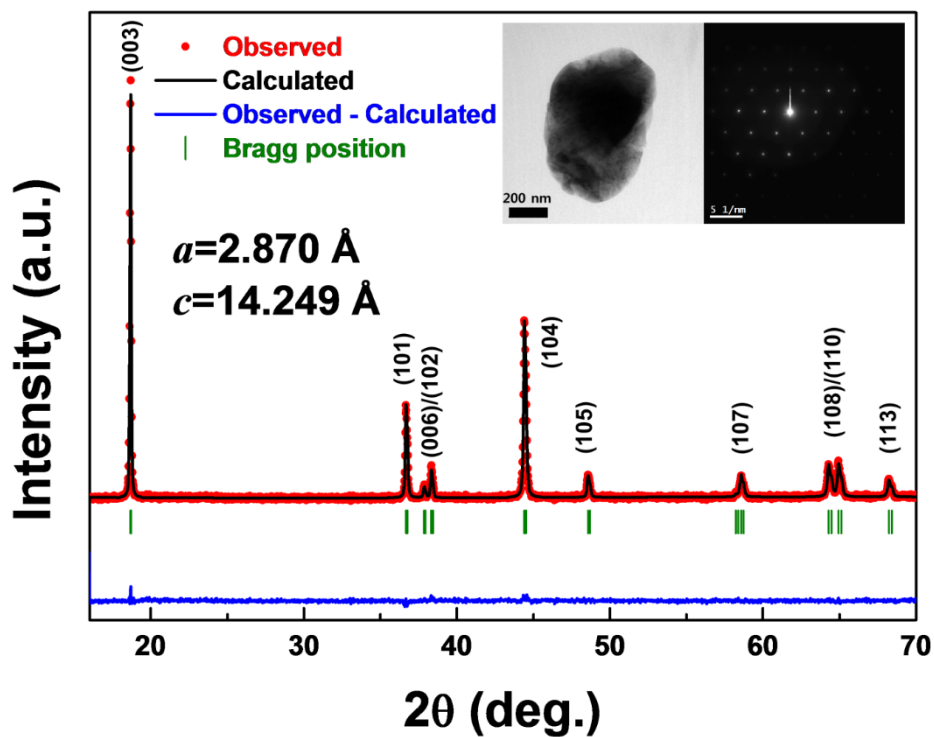


Figure 5. X-ray diffraction (XRD) pattern of $\text{LiNi}_{0.5}\text{Co}_{0.2}\text{Mn}_{0.3}\text{O}_2$ indexed based on the $R\bar{3}m$. The R factors are $R_p = 1.39\%$, $R_l = 1.69\%$, and $R_F = 2.69\%$. The figure inset shows transmission electron microscopy (TEM) images and the diffraction pattern of the single particles.^[29]

4.2. Electrochemical degradation of $\text{LiNi}_{0.5}\text{Co}_{0.2}\text{Mn}_{0.3}\text{O}_2$

Three identical cells were fabricated using the NCM523 cathode and operated at various voltage windows; 3.0 - 4.3 V, 3.0 – 4.5 V and 3.0 – 4.8 V. Figure 6a and 6b show that increasing charge cut-off voltages leads to higher reversible capacities for a few initial cycles but faster capacity degradation. While NCM523 could deliver cycle retention around 95 % after 50 cycles with 4.3 V operation, the discharge capacity decreased to 72 % and 61 % of the first capacity with 4.5 V and 4.8 V operations, respectively.

To confirm the effect of transition metals dissolution in electrolyte on capacity retention, the amounts of Ni, Co, and Mn ions in electrolyte were measured. Transition metal dissolution could contribute to capacity decay, if NCM cathode was exposed for a long time at high voltage (>4.5 V).^[30] However, the amounts of transition metal ions in electrolyte of 4.3-V, 4.5-V, and 4.8-V cycled samples were similar, which indicates that the main cause of NCM523 degradation at high voltage was not related with transition metal dissolution.(Table 1)

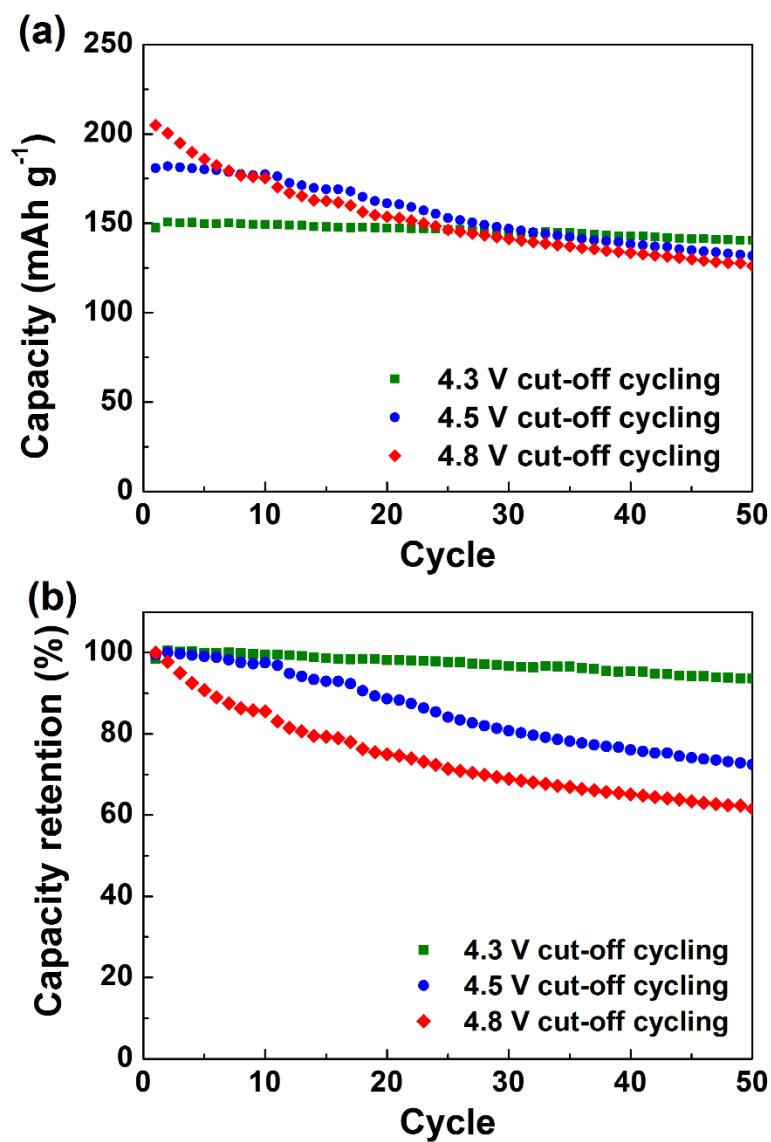


Figure 6. (a) Cycle performance and (b) discharge capacity retention at various cutoff voltages during 50 cycles.^[29]

Table 1. Concentration of Ni, Co and Mn ions in electrolyte after 50 cycles at different cutoff voltages.^[29]

	Ni ($\mu\text{g/L}$)	Co ($\mu\text{g/L}$)	Mn ($\mu\text{g/L}$)
4.3 V	1.02 \pm 0.05	1.14 \pm 0.06	4.20 \pm 0.20
4.5 V	1.26 \pm 0.06	1.17 \pm 0.06	4.02 \pm 0.21
4.8 V	0.95 \pm 0.05	1.11 \pm 0.06	4.27 \pm 0.20

Electrochemical impedance spectroscopy measurement in Figure 7a clearly reveals the relationship between impedance change and the degree of cycle degradation. Although as-prepared electrode exhibited one semi-circle in Figure 7(a), which corresponds to the charge transfer resistance (R_{ct}), all the others after cycling showed two semi-circles which are attributed to R_{ct} and the additional surface film resistance (R_f). The R_f resistance is generally caused by the formation of insulating SEI(Solid Electrolyte Interphase) layer, or the deposition of organic compounds on the surface of the electrode by the electrolyte decomposition.^[31, 32] From the inset of Figure 7(a), R_f of 4.8 V-cycled sample shows about twice larger resistance than those of 4.3 or 4.5 V-cycled samples. This may indicate a thicker surface film has formed during cycling at 4.8 V. In contrast to the relatively small variation in R_f among samples, R_{ct} undergoes substantially larger increase during cycling at high voltages. At high voltages, the R_{ct} increases by two times to ten times larger than that of the as-prepared electrode at 4.5 V and 4.8 V respectively, while 4.3 V-cycled sample showed nearly identical R_{ct} to that of as-prepared electrode. All the values of resistance are listed in Table 2. The supplementary electrochemical cycling of samples after 50 cycles at slower current rate revealed that the capacity nearly recovers to the initial capacity indicating that the electrode material remains electrochemically active even

after cycling. (Figure 8) It implies that the cycle degradation at high voltage is closely correlated with the increase in charge transfer resistance of the electrodes. In the following, the origin of the increased charge transfer resistance of the high voltage cycled samples is discussed through detailed analyses in both respects of bulk and surface structure.

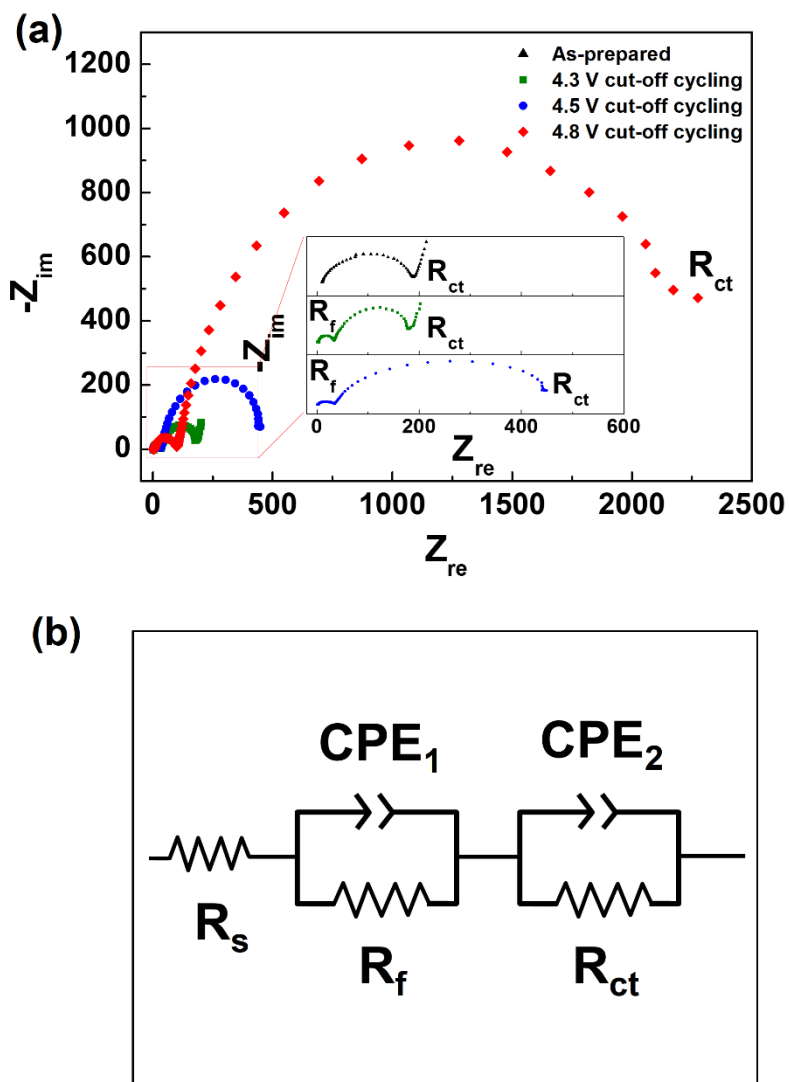


Figure 7. (a) Electrochemical impedance spectroscopy (EIS) profiles of electrodes in coin cells of the as prepared sample and samples after 50 cycles. (b) Equivalent circuit for electrodes. R_s : solution resistance; R_f : surface film resistance; R_{ct} : charge transfer resistance.^[29]

Table 2. Resistance values of as-prepared and cycled samples obtained from equivalent circuit in Figure 7b.

	R_s (Ω)	R_f (Ω)	R_{ct} (Ω)
As-prepared	11.25	-	175.65
	(1.90 %)		(2.12 %)
4.3 V	3.83	28.12	171.2
	(2.41 %)	(1.41 %)	(2.97 %)
4.5 V	3.06	29.38	465.5
	(3.99 %)	(1.56 %)	(2.53 %)
4.8 V	9.72	84.82	2305.2
	(4.19 %)	(2.04 %)	(5.40 %)

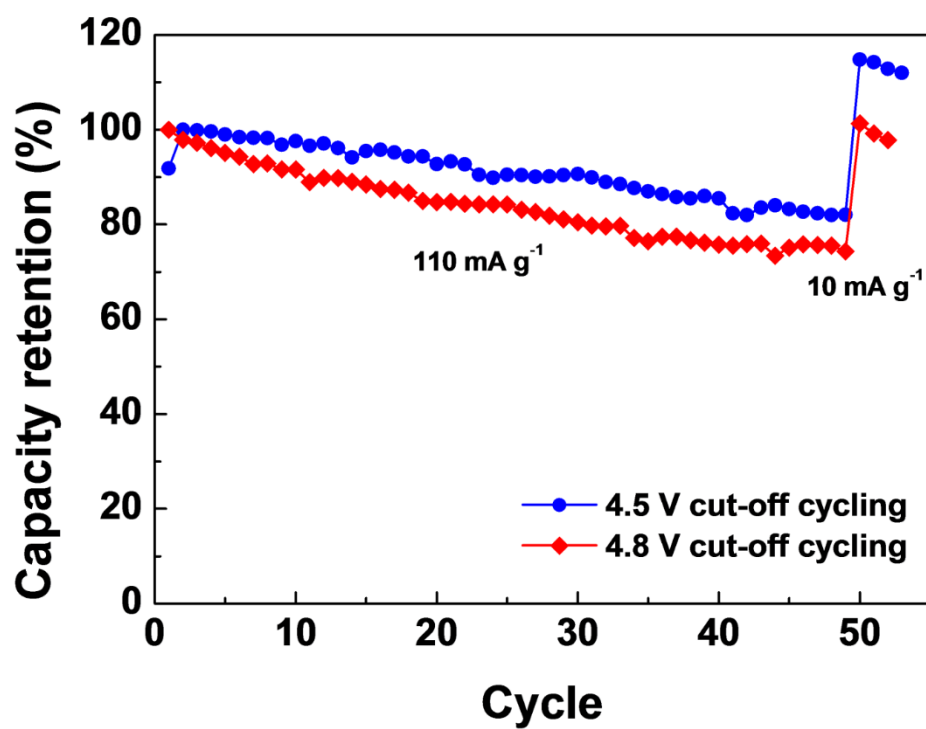


Figure 8. Recovered capacity retention after 50 cycles at a slower current rate (10 mA g⁻¹).^[29]

4.3. Structural analysis

To investigate the origin of the accelerated capacity fading above the 4.5 V cutoff, bulk structure after cycling was examined first. Each sample at the discharged state after 50 cycles, was collected and analyzed. Figure 9 compares the XRD patterns of cycled samples. Regardless of cutoff voltages, all the samples retain layered structure and do not indicate a significant structural degradation or formation of any other new phases. Slight difference in the lattice parameters were observed, but they are attributed to different amount of remaining lithium contents in each discharged samples (see the Figure 10, 11 and Table 3 for detail) The lithium deficiency in the discharged (to 3.0 V) samples implies that the electrode polarization has been built up over cycles preventing a full lithiation of the cathode even at 3.0 V. It should be also noted that higher lithium deficiency was observed for samples that was operated at higher voltage. This indicates that the electrode polarization becomes more severe when cycled at high voltages in consistent with the higher impedance value observed in Figure 7(a). In the following, factors that inhibited full lithium insertion and extraction particularly after high voltage cycles are investigated with a focus on the surface structural analysis.

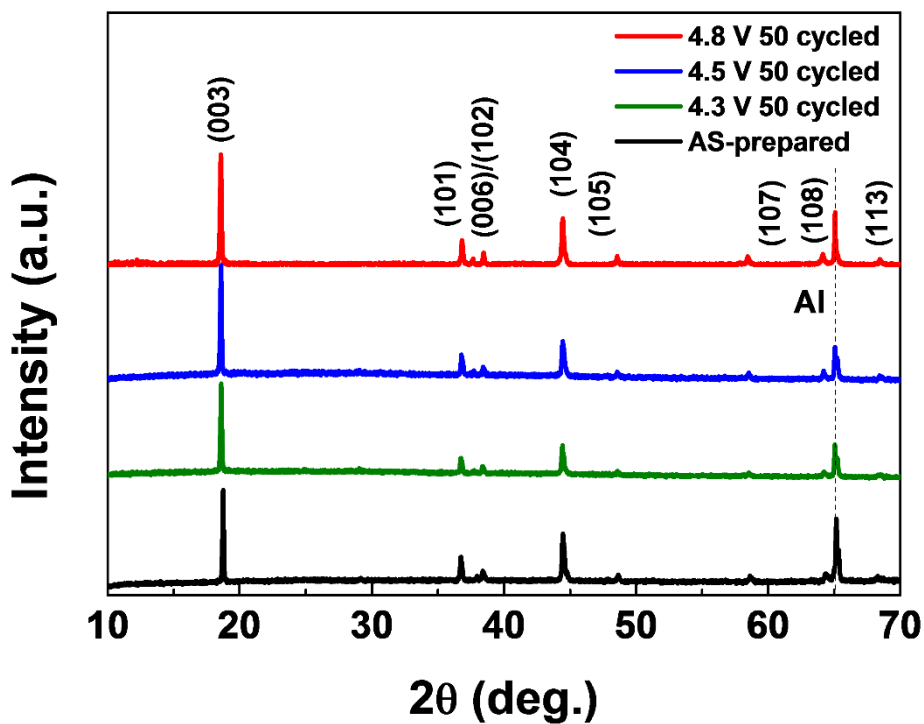


Figure 9. X-ray diffraction (XRD) patterns of the as-prepared electrode before and after 50 cycles.^[29]

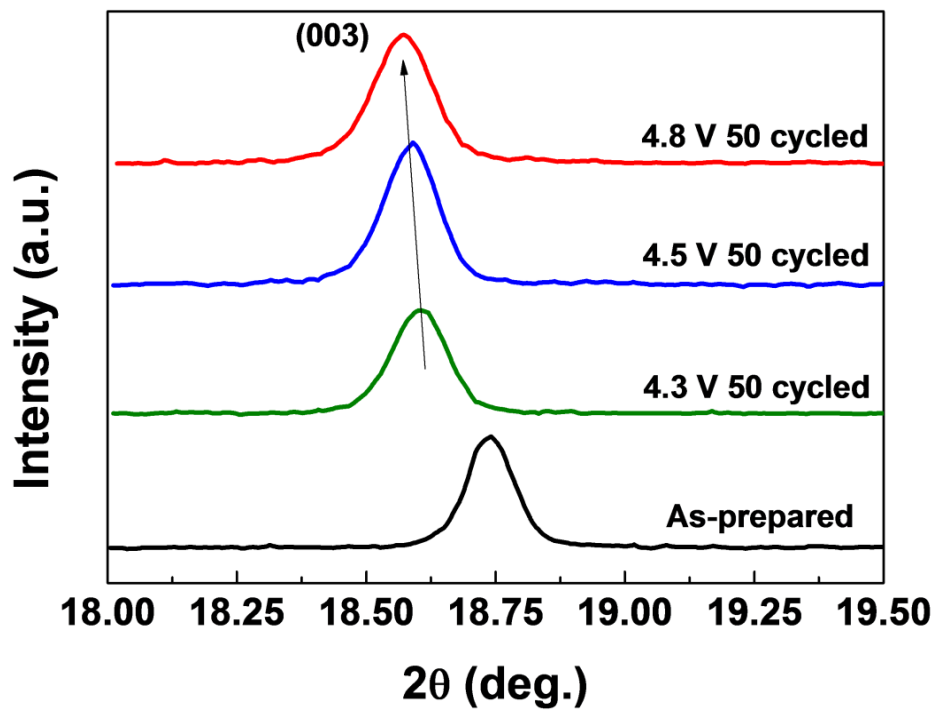


Figure 10. Magnified x-ray diffraction (XRD) patterns of Figure 9 around $2\theta = 18 \sim 19^\circ$ ^[29]

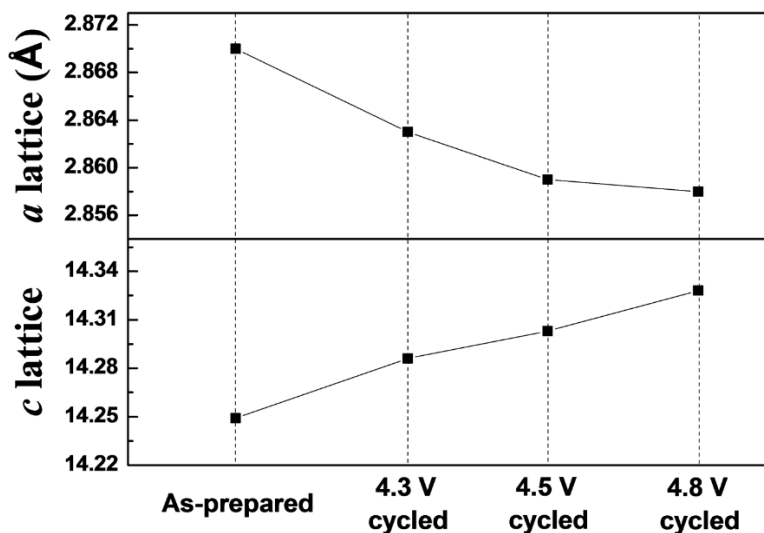


Figure 11. Lattice parameter changes of the electrodes as-prepared and after 50 cycles.^[29] The refinement of the lattice parameters of the samples revealed that the *a* lattice parameter decreased and the *c* lattice parameter increased with increasing cutoff voltage compared with those of the as-prepared material. Continuous change of the lattice parameters occurred without degradation to the layered framework. This indicates that the remaining Li contents in each discharged sample varied among the samples and was dependent on the cutoff voltage.^[33] As the Li content decreased in the layered structure material, the *a* lattice parameter typically decreased due to the smaller ionic radius of the transition metal as a result of oxidation. In contrast, the *c* lattice parameter increased because the Li deficient state created a stronger electrostatic repulsion between the two opposing oxygen layers across the Van der Waals gap.^[34, 35]

Table 3. Lattice parameters of as-prepared and cycled samples of Figure

11^[29]

	a (Å)	c (Å)
As-prepared	2.870	14.249
4.3 V	2.863	14.285
4.5 V	2.859	14.304
4.8 V	2.858	14.328

In order to probe local structural change of the samples, TEM analyses were performed. Selected area diffraction patterns (SAED pattern) were acquired from both bulk and surface regions of 4.8 V cycled sample in Figure 12. The hexagonal diffraction spots were clearly detected from the bulk region without any other trace of second phase in Figure 12(a), which is consistent with the XRD results. However, additional diffraction spots were detected at the surface region. For the clarity, the peak intensity was integrated following the bright lines in the inset of figure, which indicates the presence of additional peak. Additional diffraction spots could be indexed as (-220)s and (11-1)s in a spinel phase. The partial phase transformation from layered structure to spinel in this material is reminiscent of commonly observed layer to spinel transformation of layered LiMnO_2 during electrochemical cycling.^[8, 36] In general, layered materials prone to transform to the spinel with a thermodynamic driving force when the lithium contents are around half in the original layered structure.^[37] While the ease of layered to spinel phase transformation of $\text{Li}_{0.5}\text{MO}_2$ (M=transition metal) is dependent on the values of octahedral site stabilization energy (OSSE) of transition metal, Ni, Co, and Mn ions in NCM materials have been regarded as stable against the migration that is required for phase transformation.^[38] Thus, the partial phase transformation in the surface region was attributed to

the prolonged Li deficiency near the surface of the NCM523 which is generally observed in layered cathode material, even in the discharged state.^[39, 40] The surface lithium deficient state can be easily formed during electrochemical cycling as was shown in $\text{LiNi}_x\text{Co}_y\text{Al}_{1-x-y}\text{O}_2$ layered cathode material.^[40]

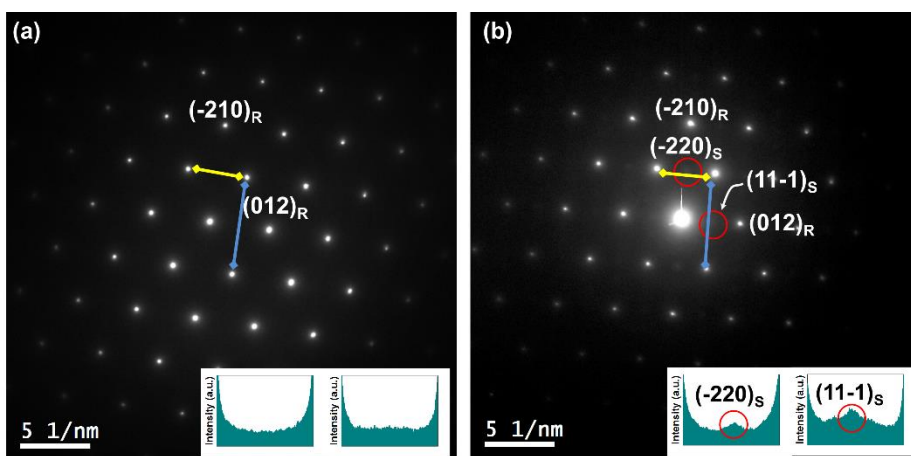


Figure 12. Diffraction patterns at the zone axis $[-1-21]_R$ after 50 cycles under 3.0–4.8 V conditions for the (a) bulk and (b) surface regions. The figure insets show bright intensity maps of the spots along yellow and blue lines. R represents a peak from the layered phase; S represents peaks from the spinel phase.^[29]

Extensive HR-TEM and fast Fourier transformation (FFT) study was done to confirm the range where the phase transformation occurred. In order to avoid misinterpretation, various regions in the sample were examined, which led to consistent results. Figure 13(a) shows the representative structural change in the NCM cycled at 4.8 V cutoff. The change in the structure is mainly localized on the surface (Figure 13(c)), while bulk region remains as rhombohedral phase (Figure 13(c)). Diffraction spots from spinel phase were detected in '2' region along with layered structure, which is consistent with SAED pattern in Figure 12(a) and 12(b). The spinel phase was continuously observed around 12 ~ 15 nm ranges of the surface. Notable is that in a very narrow region close to the surface, cubic phase begins to appear with 2 – 3 nm depth of the surface as determined by the lattice images and FFTs in Figure 13(d) and (e). In '3' and '4' regions, only two strong diffraction spots were detected. The reduction of diffraction spots is high symmetry rocksalt phase. The d-spacing of rocksalt phase acquired from the lattice image and FFT was around 2.45 Å. It is comparable to those of (11-1) planes of the NiO rocksalt phase (2.42 Å) and CoO (2.46 Å). At this moment, it is not clear whether the observed rock salt phase is NiO or CoO. But from the lattice parameter (2.45 Å) that lies between those of NiO (2.42 Å) and CoO (2.46 Å) we speculate that it is likely be the solid solution between NiO and

CoO. The probe of local environments from EELS(Electron Energy Loss Spectroscopy) measurement further indicates the formation of rocksalt phase. EELS spectra of O-K edge of as-prepared and tested electrodes were collected. The oxygen EELS peaks in supporting information Figure 14 show that two different oxygen local environment notably arises when cycled 4.8 V. Main oxygen EELS peak was observed broadly at 547 eV in both as-prepared and 4.5 V-cycled samples with similar shapes. However, oxygen peak is clearly split into two peaks of 547 eV and 543 eV after 4.8 V cycling. Split peak of around 543 eV corresponds to the characteristic oxygen peak of NiO. This observation agrees with the formation of rock salt phase confirmed by TEM results. The formation of rocksalt phase of in NCM523 during 4.8 V operation is somewhat similar to the general characteristics of Ni-rich layered systems such as $\text{LiNi}_{0.73}\text{Co}_{0.17}\text{Al}_{0.10}\text{O}_2$ that tends to form a NiO on the surface after cycle test.^[39] In layered cathode materials, rocksalt phase can be formed through the oxygen evolution when $\text{Co}^{3+/4+} t_{2g}$ or $\text{Ni}^{3+/4+} e_g$ orbital substantially overlap with oxygen 2p orbital.^{[34,}

^{41]} Oxygen evolution in NCM523 is also quite feasible at high voltage operation where Ni and Co are in highly oxidative environment.

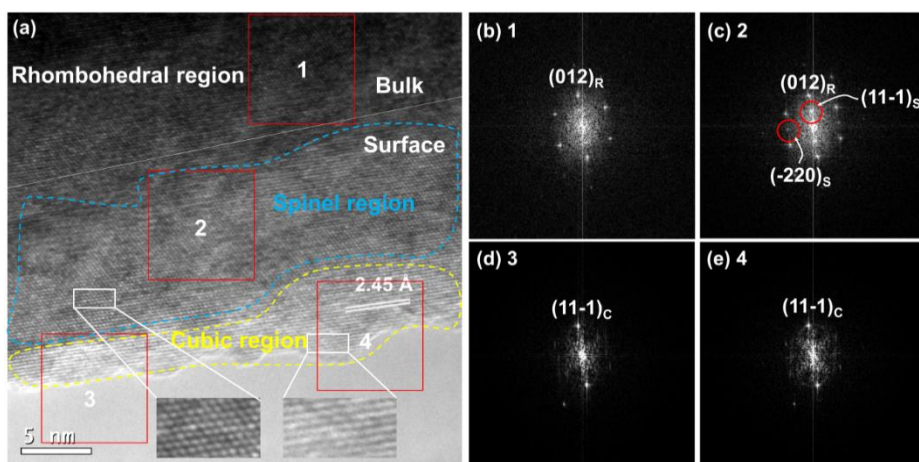


Figure 13. High-resolution transmission electron microscopy (HR-TEM) images and fast Fourier transforms (FFTs) after 50 cycles under 3.0–4.8 V conditions. (a) Lattice image of the surface region where (b)–(e) correspond to the FFTs of Regions 1–4, respectively. $(11-1)_c$ is the diffraction spot of the rock salt phase of the metal monoxide.^[29]

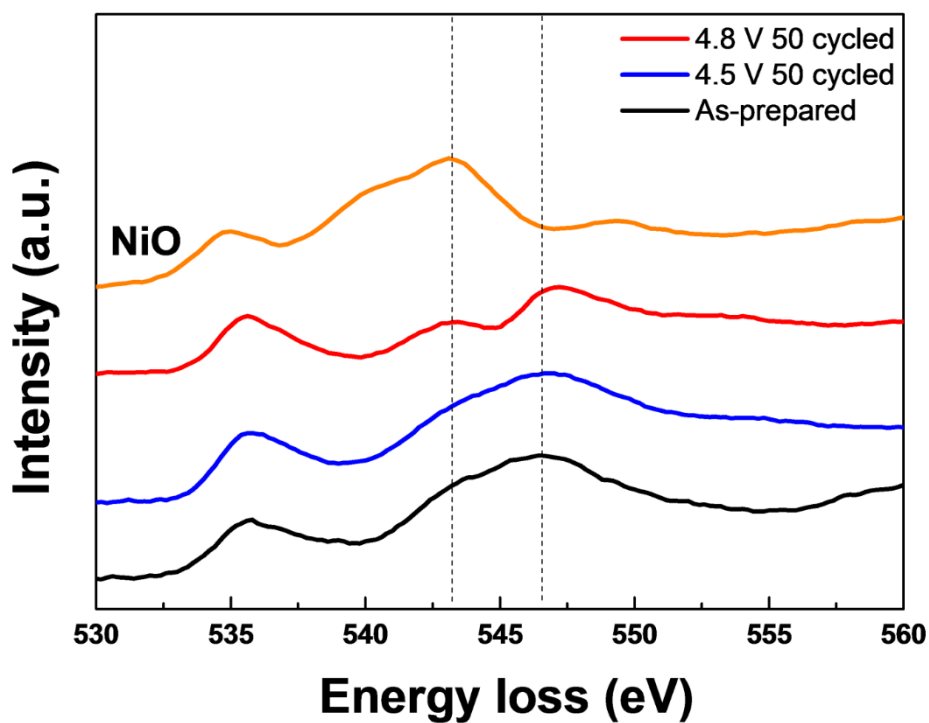


Figure 14. Electron energy loss spectroscopy (EELS) at the O–K edge of the as-prepared sample, the 4.5-V cutoff sample, and the 4.8-V cutoff sample.

The spectra were measured within a few nanometers of the surface.^[29]

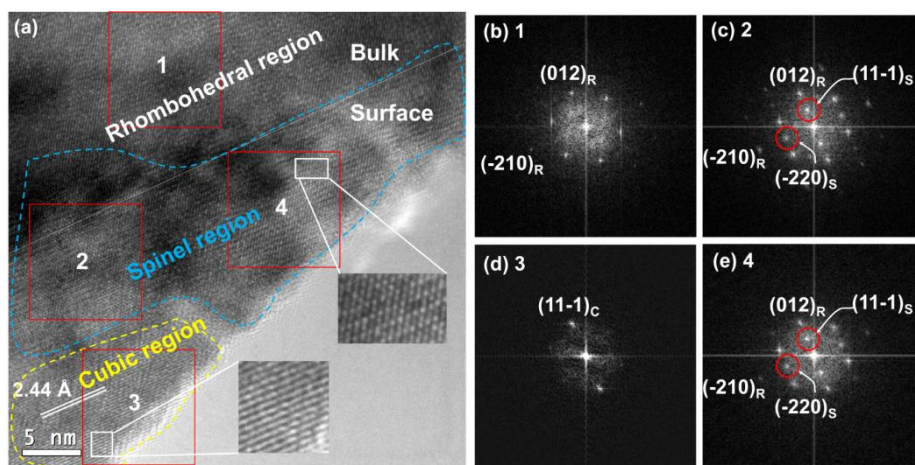


Figure 15. HR-TEM images and FFTs after 50 cycles under 3.0–4.5 V conditions. (a) Lattice image of the surface region where (b)–(e) correspond to the FFTs of Regions 1–4, respectively.^[29]

The rocksalt and spinel phases were also detected at the surface of 4.5 V-cycled sample in Figure 15. However, from the extensive sample examination, we found that the range of cubic and spinel phases differ between 4.5 V-cycled sample and 4.8 V-cycled sample. In 4.5 V sample, the cubic region was only partially shown up, and the spinel phase mainly took the outermost surfaces. It is contrast to the 4.8 V-cycled sample where cubic phase continuously encircle the spinel phase. It implies that the higher charge cut-off voltage condition promotes further the formation of cubic phase during the cycling. Exceptionally oxidative environment imposed by high voltage change is likely trigger a severe oxygen evolution from the electrode and induce the phase transformation. It is noted that the 4.3 V-cycled material did not show any trace of phase transformations contrary to 4.5 and 4.8 V-cycled electrode (Figure 16 and 17).

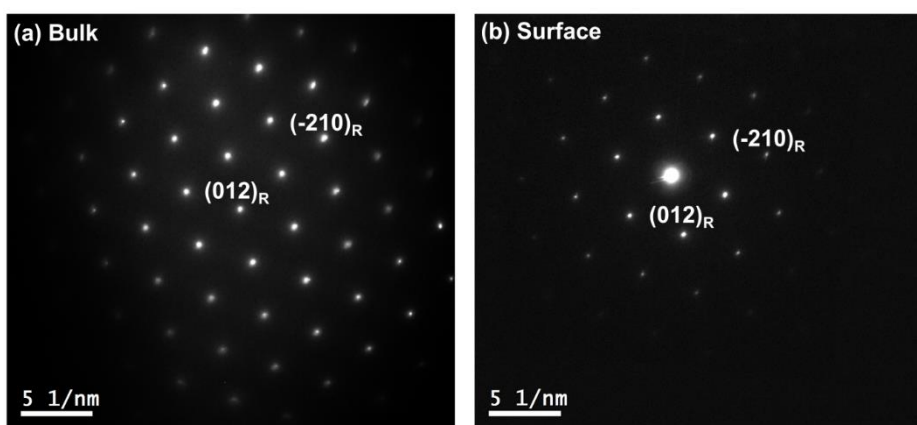


Figure 16. Diffraction patterns at zone axis $[-1-21]_R$ after 50 cycles for the voltage range of 3.0–4.3 V for the (a) bulk and (b) surface regions.^[29]

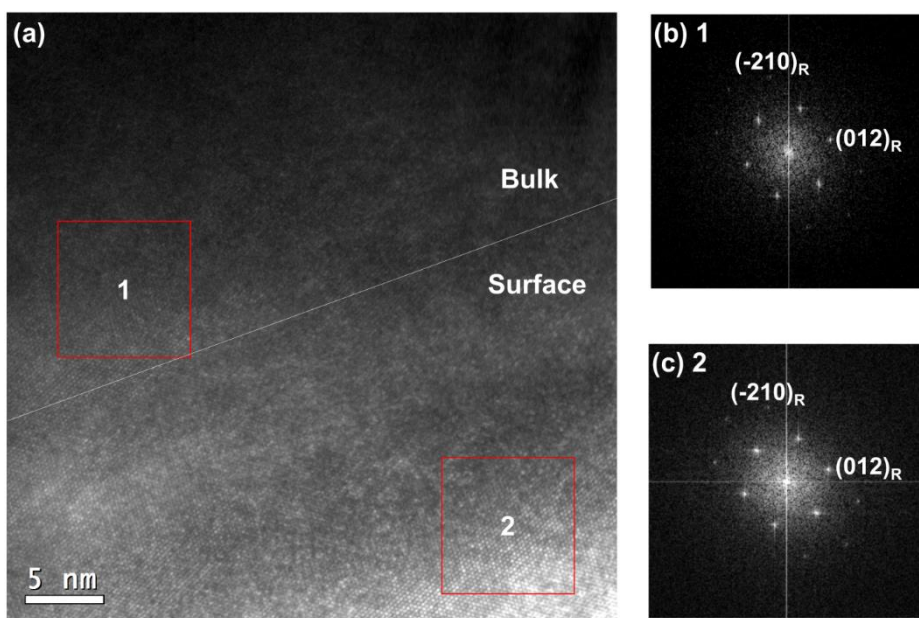


Figure 17. (a) High-resolution transmission electron microscopy (HR-TEM) images and fast Fourier transforms (FFTs) after 50 cycles in the 3.0–4.3 V range. (b) and (c) FFTs of Regions 1 and 2, respectively.^[29]

4.4. Effect of current rate on structural changes

Additionally, we studied the effect of current rate on the degradation behavior and phase transformation in the surface region. The current rate was controlled as 1000 mA g^{-1} (3.63 C) which is about ten times larger than the previous condition (110 mA g^{-1} , 0.4 C). At the 3.0–4.5 V voltage range, it showed rapid capacity decay during electrochemical cycling (Figure 18). Furthermore, the phase transformation from rhombohedral to spinel on surface was more extensively detected on the surface. The spinel phase occupied larger area (30–35 nm) than the case of 110 mA g^{-1} current rate (15–20 nm) 4.5-V cycled electrode (Figure 19). This indicates that high current rate at high voltage promotes the degradation and phase transformation on the surface.

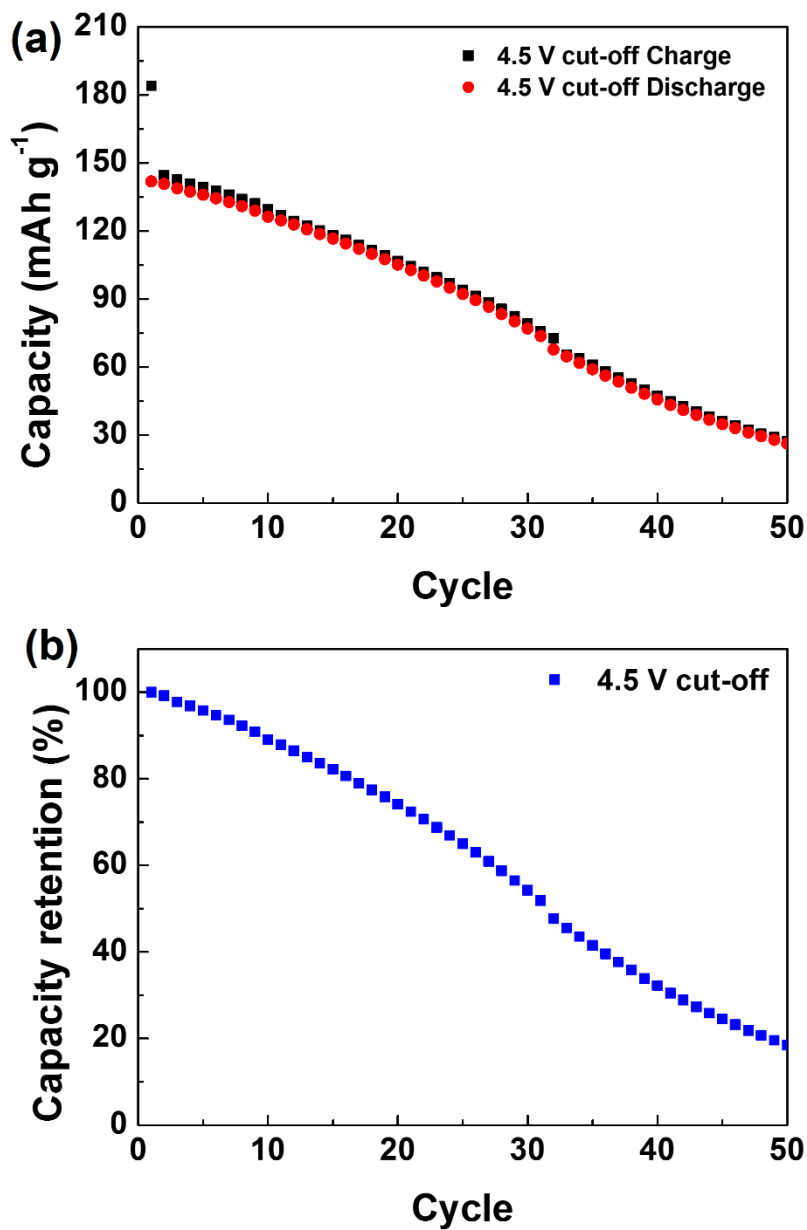


Figure 18. (a) Cycle performance and (b) discharge capacity retention at 1000 mA g⁻¹ in 3.0–4.5 V voltages during 50 cycles.^[29]

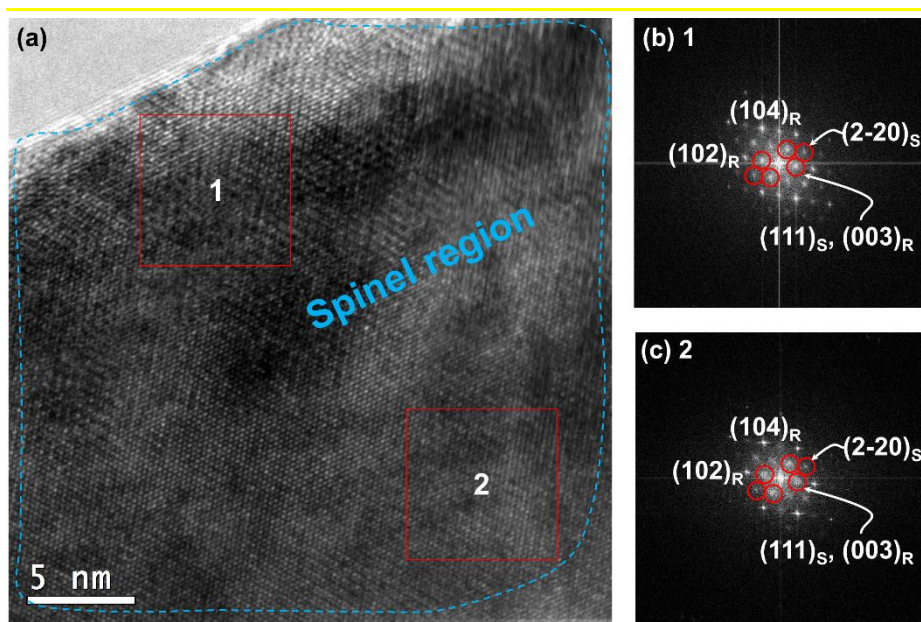


Figure 19. (a) HR-TEM image at the zone axis $[010]_R$ after 50 cycles at 1000 mA g⁻¹ in the 3.0–4.5 V range and (b), (c) FFT of the region 1, 2.^[29]

4.5. Degradation mechanisms of $\text{LiNi}_{0.5}\text{Co}_{0.2}\text{Mn}_{0.3}\text{O}_2$

The degradation mechanism of NCM523 is rather different from the previous reports on that of NCM111. It was shown that the capacity fading of NCM111 accompanies the phase transformation of O3 to O1 phase at highly charged state via the generation of stacking faults between two phases.^[34, 42, 43] However, NCM523 did not show any evidence of the O1 phase both during the cycling and at highly delithiated state. This is clearly shown in the TEM result in the supporting information.(Figure 20) It implies that the degradation mechanisms of NCM material can vary with the compositions of Ni, Co, and Mn and should be carefully considered. Based on the results from above, we propose the degradation mechanisms of $\text{LiNi}_{0.5}\text{Co}_{0.2}\text{Mn}_{0.3}\text{O}_2$ during cycling at high voltages, which were depicted in Figure 21. When the NCM523 electrode is cycled with 4.5 V cutoff, surface of the electrode suffers from phase transformation mainly to spinel phase with a trace of rocksalt formation. If the cutoff voltage increases to 4.8 V, highly oxidative environment promotes the formation of rocksalt phase more universally than 4.5 V condition and the rocksalt phase encircles the spinel and rhombohedral phases. The ranges of phase transformed region were nearly same (15 ~ 20 nm) for both with 4.8 V and 4.5 V condition but with varying fraction of spinel and

rock salt phase. We believe that these transformed phases would act as a critical factor in increasing the charge transfer resistance. The presence of ionically blocking rocksalt phase will inhibit the motion of Li ions. The variation of charge transfer resistances in Figure 7(a) between at 4.5 V and 4.8 V condition is believed to be caused by that rocksalt phase existed more on surface of 4.8 V samples than 4.5 V samples.

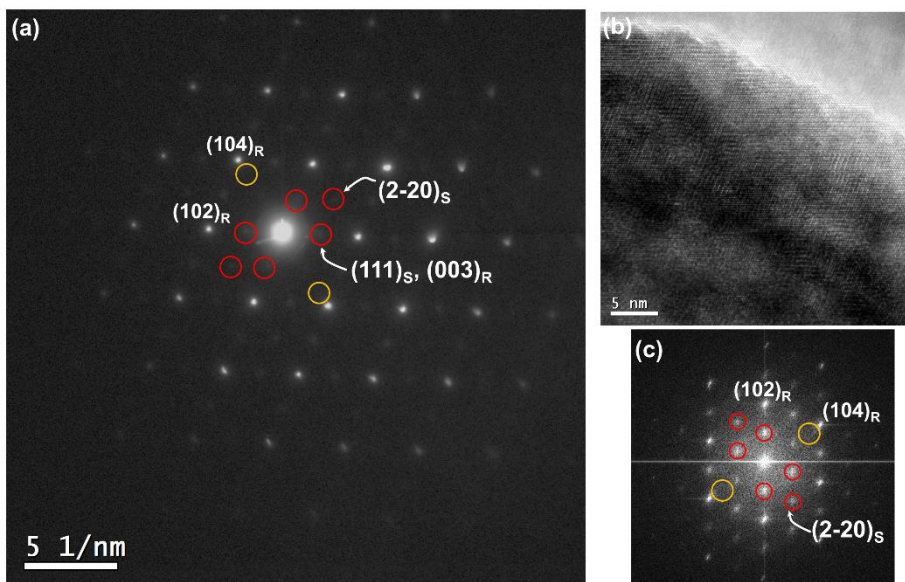


Figure 20. (a) Diffraction patterns of the zone axis $[010]_R$ after 50 cycles in the 3.0–4.8 V range. (b) HR-TEM image and (c) FFT of the (b) region. The yellow circle shows the position of the O1 phase (-202) in which no spot was shown. The red circle corresponds to the position of the spinel structure.^[29]

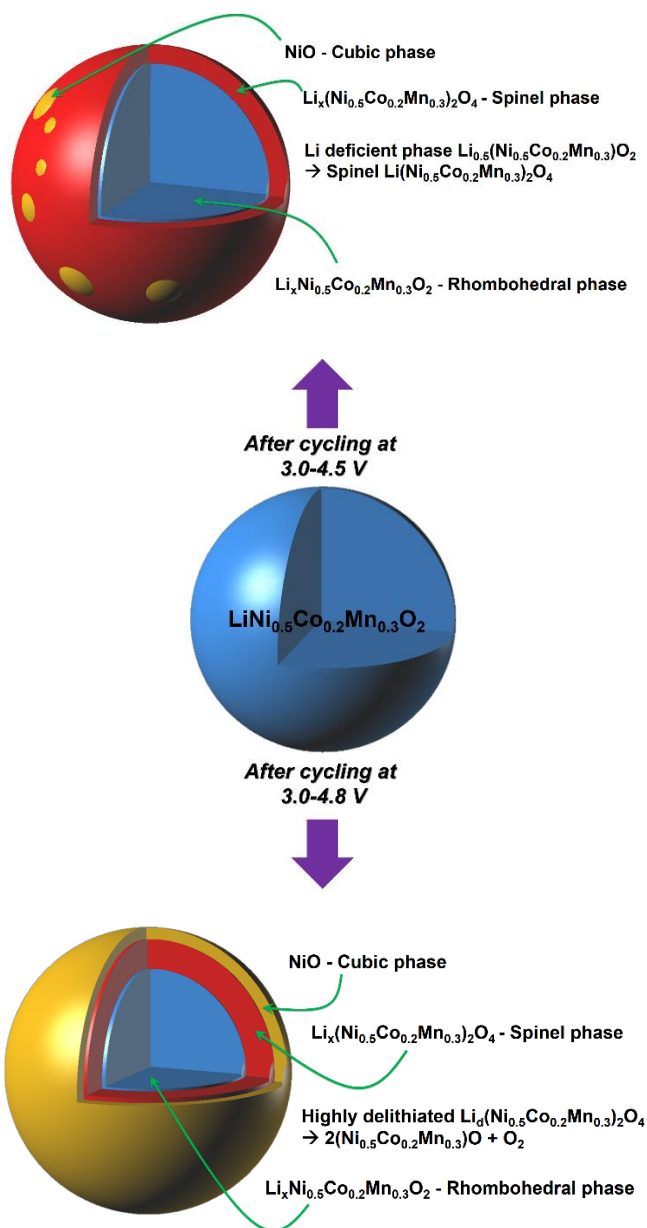


Figure 21. Degradation mechanisms of $\text{LiNi}_{0.5}\text{Co}_{0.2}\text{Mn}_{0.3}\text{O}_2$ and phase transformation after cycle tests under high-voltage conditions.

Chapter 5. Conclusion

In NCM523 materials, although global phase transformation was not detected by XRD, local structural changes were confirmed by TEM on the surface of the single particle during cycling at high cut-off voltages. Phase transformation from rhombohedral to spinel occurred, which is well known in layered material system at lithium deficient state and the formation of rock salt phase was founded partially. These transformed regions acted as electrochemically inactive part and sluggish kinetic factor. The ranges of those regions were determined by the cut-off voltages. At 4.5 V condition, spinel phase was mainly formed with slight rock salt phase. At 4.8 V, meanwhile, spinel and rock salt phases were formed widely together. The rock salt phase is the critical sluggish kinetic factor. These are different with the degradation mechanism of NCM111 which is cause by the formation of O1 phase at highly delithiated sate. This shows that NCM material degrades in different way as the components ratio of transition metals. This research can be the guide line for seeking the method to secure the stable cycle ability and to acquire large reversible capacity at the same time in Ni, Co, and Mn three component layered cathode materials.

Reference

- [1] J. M. Tarascon, M. Armand, *Nature* **2001**, *414*, 359.
- [2] M. Armand, J. M. Tarascon, *Nature* **2008**, *451*, 652.
- [3] K. Kang, Y. S. Meng, J. Breger, C. P. Grey, G. Ceder, *Science* **2006**, *311*, 977.
- [4] B. Kang, G. Ceder, *Nature* **2009**, *458*, 190.
- [5] J. N. Reimers, J. R. Dahn, *J. Electrochem. Soc.* **1992**, *139*, 2091.
- [6] A. R. Armstrong, P. G. Bruce, *Nature* **1996**, *381*, 499.
- [7] A. Rougier, P. Gravereau, C. Delmas, *J. Electrochem. Soc.* **1996**, *143*, 1168.
- [8] A. R. Armstrong, A. J. Paterson, A. D. Robertson, P. G. Bruce, *Chem. Mater.* **2002**, *14*, 710.
- [9] T. Ohzuku, A. Ueda, M. Nagayama, *J. Electrochem. Soc.*

1993, 140, 1862.

[10] T. Ohzuku, Y. Makimura, *Chem. Lett.* **2001**, 30, 642.

[11] N. Yabuuchi, T. Ohzuku, *J. Power Sources* **2003**, 119–121, 171.

[12] Z. Liu, A. Yu, J. Y. Lee, *J. Power Sources* **1999**, 81–82, 416.

[13] S. B. Kim, K. J. Lee, W. J. Choi, W. S. Kim, I. C. Jang, H. H. Lim, Y. S. Lee, *J Solid State Electrochem* **2010**, 14, 919.

[14] Y.-S. Lee, D. Ahn, Y.-H. Cho, T. E. Hong, J. Cho, *J. Electrochem. Soc.* **2011**, 158, A1354.

[15] T. Liu, S.-X. Zhao, K. Wang, C.-W. Nan, *Electrochim. Acta* **2012**, 85, 605.

[16] H. G. Song, Y. J. Park, *Mater. Res. Bull.* **2012**, 47, 2843.

[17] W. Liu, M. Wang, X. I. Gao, W. Zhang, J. Chen, H. Zhou, X. Zhang, *J. Alloy Compd.* **2012**, 543, 181.

[18] Y. Bai, X. Wang, S. Yang, X. Zhang, X. Yang, H. Shu, Q. Wu,

J. Alloy Compd. **2012**, 541, 125.

[19] B. C. Park, H. B. Kim, S. T. Myung, K. Amine, I. Belharouak,
S. M. Lee, Y. K. Sun, *J. Power Sources* **2008**, 178, 826.

[20] Y. Huang, J. Chen, J. Ni, H. Zhou, X. Zhang, *J. Power
Sources* **2009**, 188, 538.

[21] B. Peter G., S. Bruno, T. Jean-Marie, Vol. 47, 2008, 2930.

[22] A. Van der Ven, M. K. Aydinol, G. Ceder, G. Kresse, J. Hafner,
Phys. Rev. B **1998**, 58, 2975.

[23] A. Rougier, I. Saadoune, P. Gravereau, P. Willmann, C.
Delmasa, *Solid State Ionics* **1996**, 90, 83.

[24] T. Ohzuku, A. Ueda, M. Nagayama, Y. Iwakoshi, H. Komori,
Electrochim. Acta **1993**, 38, 1159.

[25] I. Belharouak, Y. K. Sun, J. Liu, K. Amine, *J. Power Sources*
2003, 123, 247.

[26] J.-Z. Kong, F. Zhou, C.-B. Wang, X.-Y. Yang, H.-F. Zhai, H.

- Li, J.-X. Li, Z. Tang, S.-Q. Zhang, *J. Alloy Compd.* **2013**, 554, 221.
- [27] T. Roisnel, J. Rodriguez-Carvajal, *Mater. Sci. Forum* **2001**, 378-381, 118.
- [28] K. M. Shaju, G. V. Subba Rao, B. V. R. Chowdari, *Electrochim. Acta* **2002**, 48, 145.
- [29] S.-K. Jung, H. Gwon, J. Hong, K.-Y. Park, D.-H. Seo, H. Kim, J. Hyun, W. Yang, K. Kang, *Adv. Energy Mater.* **2013**, n/a.
- [30] H. Zheng, Q. Sun, G. Liu, X. Song, V. S. Battaglia, *J. Power Sources* **2012**, 207, 134.
- [31] D. Zhang, B. S. Haran, A. Durairajan, R. E. White, Y. Podrazhansky, B. N. Popov, *J. Power Sources* **2000**, 91, 122.
- [32] J. Hong, H.-D. Lim, M. Lee, S.-W. Kim, H. Kim, S.-T. Oh, G.-C. Chung, K. Kang, *Chem. Mater.* **2012**, 24, 2692.
- [33] J. Shim, R. Kostecki, T. Richardson, X. Song, K. A. Striebel, *J. Power Sources* **2002**, 112, 222.

- [34] J. Choi, A. Manthiram, *J. Electrochem. Soc.* **2005**, *152*, A1714.
- [35] J. Hong, D.-H. Seo, S.-W. Kim, H. Gwon, S.-T. Oh, K. Kang, *J. Mater. Chem.* **2010**, *20*, 10179.
- [36] J. Reed, G. Ceder, A. Van Der Ven *Electrochem. Solid State Lett.* **2001**, *4*, A78.
- [37] G. Ceder, A. Van der Ven, *Electrochim. Acta* **1999**, *45*, 131.
- [38] S. Choi, A. Manthiram, *J. Electrochem. Soc.* **2002**, *149*, A1157.
- [39] H. Kobayashi, M. Shikano, S. Koike, H. Sakaebe, K. Tatsumi, *J. Power Sources* **2007**, *174*, 380.
- [40] J. Nanda, J. Remillard, A. O'Neill, D. Bernardi, T. Ro, K. E. Nietering, J.-Y. Go, T. J. Miller, *Adv. Funct. Mater.* **2011**, *21*, 3282.
- [41] J. B. Goodenough, Y. Kim, *Chem. Mater.* **2009**, *22*, 587.
- [42] S. C. Yin, Y. H. Rho, I. Swainson, L. F. Nazar, *Chem. Mater.*

2006, *18*, 1901.

[43] K.-W. Nam, S.-M. Bak, E. Hu, X. Yu, Y. Zhou, X. Wang, L.

Wu, Y. Zhu, K.-Y. Chung, X.-Q. Yang, *Adv. Funct. Mater.* **2012**, n/a.

국문요약

NCM 계열의 배터리 소재는 기존 LiCoO_2 보다 높은 용량과 저렴한 가격으로 차세대 리튬 배터리 양극소재로 주목 받고 있다. 그러나 고용량 구현을 위한 고전압 구동시 사이클이 진행됨에 따라 용량이 빠르게 감소하는 수명특성이 큰 문제가 되고 있다. 이러한 문제점을 해결하기 위해 NCM 물질 표면특성을 개선하는 방법으로 고전압 구동시 수명특성을 향상시켜왔으나, 실제로 NCM 계열의 소재가 고전압 구동시 수명특성이 저하되는 이유에 대한 근본적인 연구는 많이 부족한 상태이다. 따라서 본 연구에서는 NCM 계열 소재 중에서 상용화 단계에 이른 물질 중 $\text{LiNi}_{0.5}\text{Co}_{0.2}\text{Mn}_{0.3}\text{O}_2$ (NCM523) 물질에 대해서 작동 전압구간에 따른 수명특성 저하 확인 및 열화메커니즘에 대한 분석을 진행하였다.

50회 충전 방전을 반복한 후 발현되는 용량을 살펴보면 3.0–4.5 V 구간에서는 초기용량의 72 %, 3.0–4.8 V 구간에서는 초기용량의 61 % 가 용량발현 되는 것을 확인하였다. 이에 대한 열화메커니즘 분석으로는 XRD와 TEM을 이용하여 구조적인 분석을 진행하였다. 그 결과, 용량감소가 발생한 이후에 NCM523

물질 표면에 스피넬과 rock salt 물질이 15 ~ 20 nm 범위로 생성되는 것을 확인 할 수 있었다. 또한 이렇게 생성된 스피넬과 rock salt 물질은 리튬 이온의 이동을 방해하게 되어 charge transfer 저항을 증가시킨다는 것을 확인 할 수 있었다. 특히 rock salt 물질의 경우는 3.0-4.8 V 전압 작동 구간에서 더 많이 생성되며, 용량저하에 더 많은 영향을 끼치는 것을 확인하였다. 추가적으로 리튬이 삽입 또는 탈리 되는 속도가 빨라짐에 따라 50 사이클 이후 용량감소가 더 크게 발생하며, 표면에 생성되는 스피넬과 rock salt 물질의 영역이 20 ~ 30 nm 로 조금 더 확장된 형태로 나타난다는 것을 확인하였다. 이러한 열화 메커니즘은 $\text{LiNi}_{1/3}\text{Co}_{1/3}\text{Mn}_{1/3}\text{O}_2$ (NCM111) 물질에서 나타나는 열화메커니즘(O3 구조에서 리튬 삽입 및 탈리의 가역성이 떨어지는 O1 구조로의 변화)과는 다르게 나타났다. 따라서 같은 NCM 계열의 소재더라도 각각의 물질의 열화메커니즘은 다를 수 있음을 알 수 있었다.

주요어: 리튬 이온 배터리, 양극, 층상형 구조, 열화, 옥사이드
학 번: 2012-20633

감사의 글

대학생활을 거쳐 대학원 석사과정으로 공부한 2 년에 이르기까지 항상 따뜻한 조언으로 응원해주시고, 든든한 버팀목이 되어주신 사랑하는 아버지, 어머니, 그리고 동생 수진이에게 먼저 감사의 말씀을 드립니다. 그리고 저를 받아주시고, 아무것도 몰랐던 저를 2 년간 열정적으로 성심성의껏 지도해주신 강기석 교수님 정말 감사드립니다. 박사과정에는 교수님께서 지도해주신 2 년을 바탕으로 더욱 훌륭하고, 자질있는 연구자가 될 수 있도록 열심히 노력하겠습니다.

2 년의 기간 동안 가장 많은 시간을 같이 보낸 연구실 선배님들과 후배님들 그리고 동기들에게도 감사하다는 말씀 드리고 싶습니다. 지금은 졸업 하신지 오래되신 분들이지만, 처음 입학한 저에게 책임감과 많은 가르침을 주신 김성욱 박사님, 항상 따뜻하게 챙겨주시고 연구실 생활에 모범이셨던 서동화 박사님께 감사드립니다. 그리고, 지금 연구실 생활을 함께하고 있는 윤영수 박사님, 삶의 지혜를 배울 수 있었던 혁조형, 얼마 전 박사님이 되신 종순이형, 짧은 머리도 잘 어울리시는 진수형, 연구자의 모범 영욱이형, 똑똑한 지현이형, 성실한 해겸이형,

분위기메이커 규영이형, 자유로운 인철이형, 소녀감성 형섭이형,
내기를 좋아하는 희대형, 번역기 병주형, 조용한 인경이,
느리지만 착실한 영준이형, 친구 따라 강남간 교진이, 홍일점이
된 현아, 엘리트 갑인이, 부지런한 인상이까지 모두에게 감사의
말씀을 드립니다.

2 년간 AEML 덕분에 많이 배우고, 많이 성장 한 것 같습니다.
앞으로 새로 시작할 4~5 년의 공부에서도 후배로서, 선배로서
책임과 역할을 다하며 연구자로서 크게 성숙될 수 있도록
노력하겠습니다.

모든 분들께 감사드립니다.